A Pressure-Amplifying Monopropellant Engine for Actuator-Localized Pneumatic Power

Samuel Dutra Gollob[1], Alberto Comoretto[2], Qifan Yu[1], Matthew Fernandez[1], Korebami Adebajo[1], Johannes T. B. Overvelde[2,3], Kaitlyn Becker[1], Ellen T. Roche[1,4]

2025 IEEE 8th International Conference on Soft Robotics (RoboSoft) | 979-8-3315-2020-5/25/$31.00 ©2025 IEEE | DOI: 10.1109/RoboSoft63089.2025.11020950

***Abstract*— Despite its various potential uses, untethered pneumatics have little practical use due to the speed, power, and controllability limitations of power systems, and system-design restrictions (dead volume contained in pneumatic circuits and hardware needed to handle high actuator pressures). In this work, we present a compact monopropellant engine that localizes pressure generation to actuators. Our approach minimizes dead volume by eliminating pneumatic circuitry and allows high-pressure actuation from a low-pressure fuel source. We introduce the architecture, present a hardware implementation, and prove our pressure-amplification working principle experimentally. We also experimentally demonstrate fast response time (<30ms), high-pressure capability (>100kPa), high flow rate capacity (∼140 SLM/kg), and the ability to control the rate of gas output and volume of produced gas. Finally, we interface the engine with two distinct soft actuators to demonstrate its plug-and-play ease of use, operating at both high speeds and high pressures, and estimating a promising power output range (∼5-25W/kg). With this design, we hope to move closer towards self-contained pneumatic muscles that interface with low-pressure embodied energy storage, which may increase the viability of pneumatic actuation for untethered robotic applications.**

I. INTRODUCTION

Pneumatic actuators are diverse [1] and have had a wide variety of proposed applications, from soft robotic locomotion [2], [3], [4], to wearable medical devices [5], [6] and exoskeletons [7], [8], [9]. Despite compelling untethered applications, pneumatically actuated systems struggle to reach high-performance metrics. In most assistance or locomotion applications, devices require actuation rates in the millisecond to <1s scale, with high actuator controllability [10], [11], [12], while most untethered pneumatic systems actuate in the scale of multiple seconds [3], [2] or suffer from lack of fine control [13], [14], [15], [16]. For future use in high-performance untethered pneumatic applications, we aim to develop a pneumatic power architecture with low delays, high flow rates, and high pressures, while preserving controllability and compactness.

The current trade-off between power and controllability comes from limitations in existing power sources. Pump or tank-based power architectures are controllable, but often do not provide sufficient power and flow rates for rapid actuation as on-board power options [2], [3], and pressurized tanks do not scale well in energy density as pressure or scale requirements increase [17]. Combustion-based architectures have been proposed as a high-power, energy-dense alternative, but due to their explosive nature, are restricted to short-burst actuations - not demonstrating gradual pressurization or the ability to hold pressure [13], [14], [15], [16].

Monopropellant-based pneumatic systems strike a balance, as they have demonstrated high power output and high controllability [18], [19], [20]. Because monopropellants function by generating gas from a liquid fuel, they can hold generated pressures unlike combustion-based systems. For these reasons, we chose monopropellants for our high-speed, controllable pneumatic framework.

In addition to controllability and power output, it is important to consider effective energy density and dead volume when designing a high-performance pneumatic power system. Effective energy density, as described by Whener et al. [17], considers not only the energy density of the fuel (i.e. a battery, compressed gas, or monopropellant), but also the power hardware mass (such as pumps, valves, or storage tanks) that holds and delivers the fuel as pneumatic work. Minimizing power hardware mass, while maximizing fuel energy density, is key in maximizing the effective energy density of a fuel system, and thus the system's operating time. Secondly, dead volume in the form of pneumatic circuits adds delays, efficiency losses, decreases actuation stiffness, and should be minimized as much as possible [21].

Most pneumatic systems based on pumps, tanks and monopropellants use a similar architecture, where a central high pressure source pushes gas into actuators [2], [3], [18], [19], [22], [23], [24]. We find that this approach creates unnecessary hardware mass and dead volume. The hardware mass waste comes in the form of high-pressure tanks [3], [17], [19] and accumulators [2], while the dead volume comes in the form of the same accumulators and pneumatic lines that deliver gas to the actuators [2], [3], [23], [24].

In most monopropellant systems, this centralized architecture uses a high-pressure fuel tank to push monopropellant into a catalyst in a reaction chamber [18], [19], [23], [22] - we call this a Fuel-to-Catalyst (F2C) system, as fuel flows into a catalyst. In previous work, we presented an alternative F2C concept that would reduce high upstream pressure by pushing fuel into reactors from a low-pressure fuel tank [25]. We propose that this can be explored further, by reacting and delivering gas directly into each actuator.

In this work, we present a monopropellant-based pneu-

[1] Mechanical Engineering Dept., Massachusetts Institute of Technology (MIT), Cambridge, MA, USA.
[2] Autonomous Matter Dept., AMOLF, Amsterdam, The Netherlands
[3] Mechanical Engineering Dept., Eindhoven University of Technology, Eindhoven, The Netherlands
[4] Institute for Medical Engineering and Science, MIT, USA.
Corresponding author: etr@mit.edu

Authorized licensed use limited to: MIT. Downloaded on July 04,2025 at 10:25:47 UTC from IEEE Xplore. Restrictions apply.

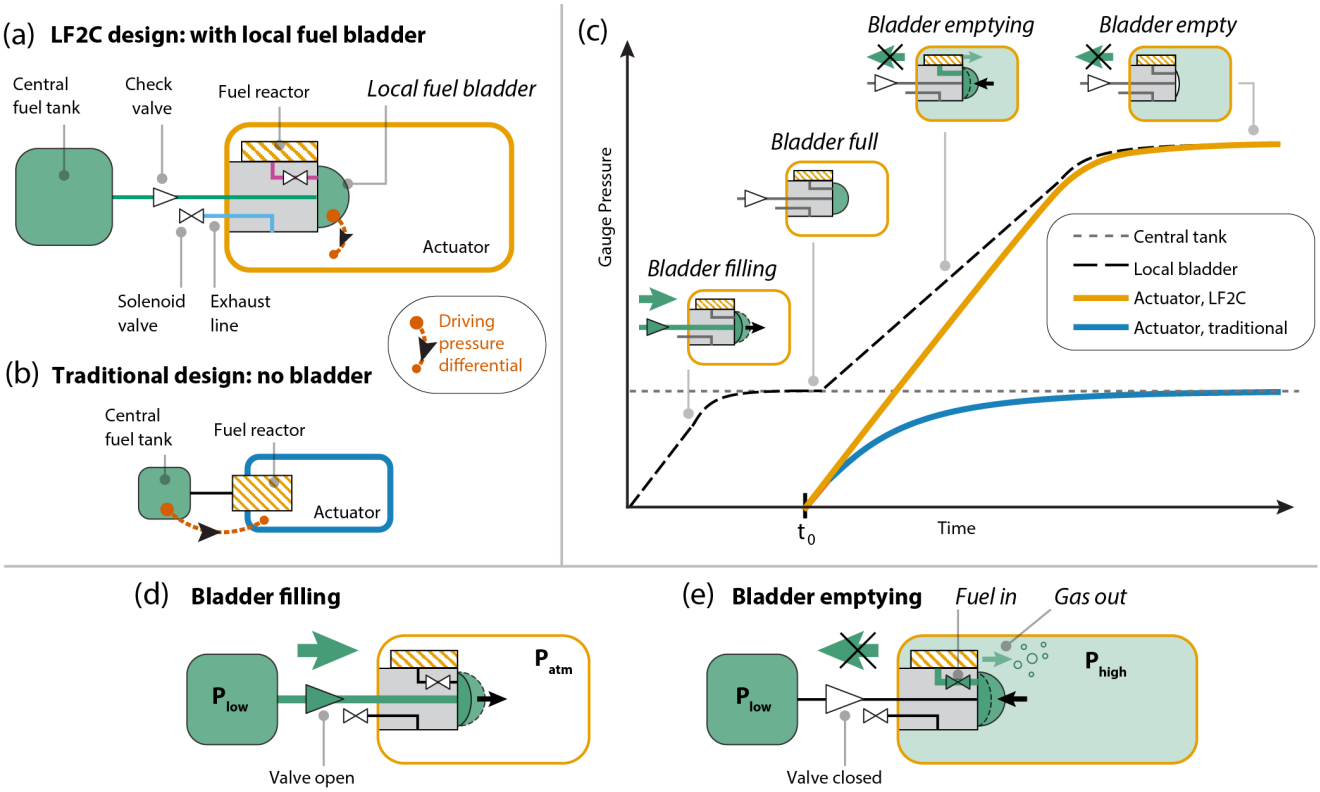

Fig. 1. **The LF2C design implements a local fuel bladder to amplify pressure, allowing actuation at pressures higher than the central fuel tank.** (a) Schematics of LF2C design and (b) a traditional propellant-based pneumatic power design, with a catalyst reactor in line with the fuel tank and actuator. The three major LF2C lines are colored: fuel line (green), reactor line (magenta), exhaust line (blue). The driving pressure differential (orange dashed line with black arrowhead) labels the two components whose pressure differential drives the motion of fuel into the reactor. (c) Schematic of the LF2C working principle, illustrating how the presence of a local bladder internal to the actuator allows the actuator to pressurize beyond the fuel tank pressure. Initially the empty bladder is filled passively by the central fuel tank. At t_0, an active valve allows fuel to flow from the bladder into the fuel reactor, pressurizing the actuator. In the case of the traditional "no bladder" design, the active valve allows fuel to flow from the central tank to the fuel reactor. (d) Close-up schematic of the bladder filling and (e) emptying stages, highlighting the pressures at the central tank and actuator, where $P_{\text{atm}} < P_{\text{low}} < P_{\text{high}}$. Note the check valve allows fuel in from the tank to the bladder, but does not allow fuel to flow from the bladder to the tank once the pressure in the actuator increases. This schematic also labels the path of fuel during the emptying phase: from the bladder into the reactor as fuel, out from the reactor into the actuator as gas.

matic engine intended for high-speed, high-pressure, and high-power delivery of pneumatic power directly to actuators. We call our approach Local Fuel-to-Catalyst (LF2C), as it is an F2C system with a key design feature: the localization of an elastic fuel bladder and fuel reactor to the inside of each actuator. This allows us to create a pneumatic actuation platform with minimal dead volume, fast response times (<30ms), high pressurization rates (∼100ms), high-pressure capability (>100kPa), high flow rate capacity (∼140 SLM/kg), high specific power (5-25W/kg), and isolation between the actuator pressure and the rest of the system, reducing power hardware mass. In addition to these benefits, the presence of a flow-regulating valve allows repeatable control of the rate and amount of released gas.

First, we present the working concept behind the LF2C architecture, then describe our hardware implementation of the LF2C engine. We then explain the hardware setup for our experimental characterization of the engine and its integration into two distinct actuators. We present the results of the system characterization, which prove its key working concept and show its controllability. We also discuss some take-aways from the actuation demonstrations shown in the supplementary video, and finally present future directions.

II. WORKING CONCEPT

The LF2C engine concept is depicted in Figure 1(a). The engine contains an elastic fuel bladder and fuel reactor (a chamber with catalyst) inside a pneumatic actuator of choice. There are three required channels. First, a fuel line (green) connects a low-pressure central fuel tank to the local fuel bladder, allowing the fuel tank to fill the bladder. The fuel line has a check valve (its role will be discussed with Figure 1(e)). Secondly, a reactor line (magenta) links the local bladder to the fuel reactor, allowing fuel to react and gas to enter the actuator. An active valve (the reactor valve) is included in this line to control the pressurization of the actuator. Finally, an exhaust line (blue) links the actuator to atmosphere through an active valve.

The traditional "no bladder" F2C design differs from the LF2C design mainly by the lack of an elastic local fuel bladder - see Figure 1(b). In the traditional design, pressure in the central fuel tank pushes fuel directly into the reactor,

Authorized licensed use limited to: MIT. Downloaded on July 04,2025 at 10:25:47 UTC from IEEE Xplore. Restrictions apply.

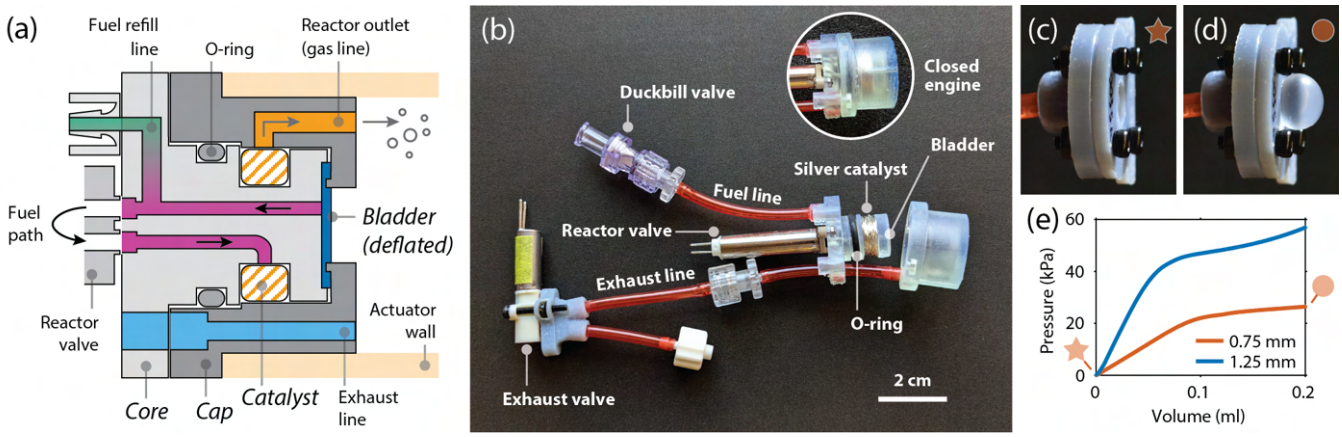

Fig. 2. **Our hardware implementation of the LF2C engine.** (a) A Schematic of the main engine component containing the three key channels: fuel line (green), reactor line (magenta) and exhaust line (blue), plus the reactor outlet (yellow), an exit for gas generated in the reactor. The engine is split into a cap piece (inside actuator) and core piece (outside actuator). (b) Photo of the assembled engine including the check valve on the fuel line (duckbill valve), reactor valve attached to main engine body, and exhaust valve on the exhaust line. (c) Image of a non-inflated elastic bladder in the bladder characterization setup. (d) Image of the inflated bladder (as would be used in the engine's local reservoir). (e) Pressure-volume curves of bladders of different thicknesses, from the bladder characterization setup.

releasing gas into the actuator. Conversely, the LF2C's elastic bladder holds fuel inside the actuator, allowing the actuator pressure to push on the bladder. This ensures the fuel flow to the reactor is driven purely by the elasticity of the local fuel bladder, and not affected by the actuator pressure. This distinction in the fuel flow pressure gradients of the two approaches is labeled as the "driving pressure differential" in Figure 1(a,b)).

The effect of these distinct driving pressure differentials is illustrated in Figure 1(c). First, an empty LF2C bladder is passively filled by the central tank. With a full bladder, at t_0, fuel is allowed to flow into the reactors of both designs. In the traditional design, fuel flows from the central tank into the reactor, pressurizing the actuator until the pressure equalizes with the tank, and no more fuel can flow to the reactor. In the LF2C design, the bladder's elastic energy pushes fuel into the reactor independently of the actuator pressure until the bladder is empty. With enough fuel in the bladder, the actuator reaches a final pressure far above the central tank pressure. For this reason, it can be useful to think of the LF2C architecture as a pressure amplifier: despite feeding the bladder from a relatively low pressure fuel source, high pressures can be reached downstream.

The bladder's filling and emptying stages are detailed in Figure 1(d,e) With the actuator at atmospheric pressure (P_{atm}) and the central tank at $P_{\text{low}} > P_{\text{atm}}$, fuel flows into the local bladder through the fuel line until the bladder's pressure equalizes with the tank (Fig. 1(d)). In the emptying stage (Fig. 1(e)), the reactor line opens and the bladder pushes fuel into the reactor. As the gas from the reactor pressurizes the actuator, the check valve in the fuel line prevents the bladder from emptying back into the central tank. The actuator is isolated from the central tank, with an internal pressure of $P_{\text{high}} >> P_{\text{low}}$. Though not depicted, opening the exhaust line would depressurize the actuator and allow the tank to passively refill the bladder. Note that a sufficiently large bladder could allow multiple actuation cycles before needing to refill.

III. MATERIALS AND METHODS

A. Hardware Implementation

We show our centimeter-scale hardware implementation the LF2C system in Figure 2. The engine has a radially-swept profile with an inner core, which contains the catalyst and most of the necessary channels, and an outer cap piece which is designed to be embedded in the actuator or pressurized system. Figure 2(a) shows how the three channels (fuel line, reactor line, and exhaust line) are incorporated in the compact architecture. An O-ring seals the interface between the core and cap and the bladder (a silicone disk) is clamped down to the top face of the core by the cap. Silver wire catalyst is spooled around the compact annular catalyst cavity, where fuel is forced to travel from the inlet, around the cavity, to the outlet on the opposite end.

The fully assembled LF2C system is depicted in Figure 2(b). The main body of the engine is printed in in Formlab's ClearV4 using a Form 3B Stereolithography printer (Formlabs). The cured resin was checked for chemical compatibility by submerging in 50% concentration hydrogen peroxide for two hours. A silicone duckbill valve (DUC FIMO, MiniValve International) is the check valve on the fuel line. For the reactor valve, we use a small-scale solenoid valve with hydrogen peroxide compatibility, low power, fast response, and sufficient pressure capabilities of 200kPa (LFNA1250125H, The Lee Company). The exhaust solenoid valve (LHDA0523112H, The Lee Company) was chosen for similar reasons. At the reactor core, approximately one gram of 0.25mm diameter silver wire (99.9% trace metal basis, Sigma-Aldrich) is spooled within the catalyst cavity. The core sealing O-ring (size 012) is made of hydrogen peroxide-compatible Viton Fluoroelastomer (McMaster-Carr). Other components with relevant hydrogen peroxide compatibility

Authorized licensed use limited to: MIT. Downloaded on July 04,2025 at 10:25:47 UTC from IEEE Xplore. Restrictions apply.

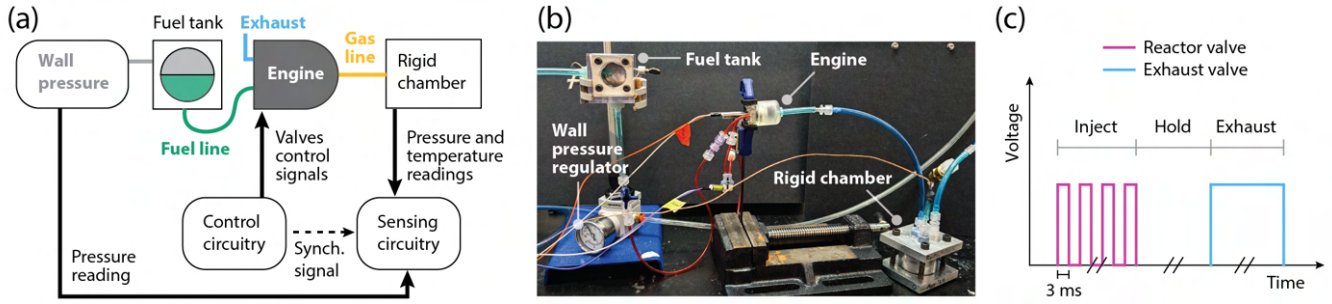

Fig. 3. **The engine characterization setup.** (a) A schematic of the engine characterization setup, illustrating how the hardware and circuitry components are connected. (b) A picture of the same characterization setup, including the fuel tank in level with the engine, wall pressure regulator for pressurizing fuel tank, and rigid sensorized chamber for receiving the engine's output. Circuitry not shown. (c) Example schematic of the valve input signals during one pressurization cycle for the experiment. The injection phase is when 3-ms voltage pulses are sent to the reactor valve at fixed intervals (i.e. a frequency), the holding phase is when the system is kept pressurised, and the exhaust phase is when the exhaust valve is fully opened.

are the 1/16in ID PVC tubing in red and the clear polycarbonate connectors seen throughout (McMaster-Carr). Insert holes printed throughout the engine allow insertion of nuts used in anchoring the valves and closing the engine. The blue mount for the exhaust valve is made from VeroBlue resin (Objet30 Prime, Stratasys Inc.), also tested for hydrogen peroxide compatibility. With all components depicted in Figure 2, the engine weighs 36 grams.

We show the inflated and deflated elastic bladder in Figure 2(c,d). To manufacture the bladder, we pour Smooth-On EcoFlex^{TM} 00-35 FAST silicone into an open mold, allowing it to cure over 5 minutes. The mold, 3D-printed in VeroBlue (Objet30 Prime, Stratasys Inc.), is a 9mm diameter cylindrical cut-out with an extruded internal ring (6mm ID, 7.5mm OD), half the height of the cut-out. The ring creates a ring-shaped notch on the bladder, which is useful for later centering and clamping in the holder (see the notch at the bladder interface in Fig. 2(a)). Four bladder thicknesses were cast, with heights of 0.5mm, 0.75mm, 1.00mm, and 1.25mm, allowing selection of bladder thickness.

To obtain the pressure-volume (P-V) curves of the bladders, we perform volume-controlled experiments using a syringe pump (PHD ULTRA^{TM}, Harvard Apparatus). Figure 2(e) shows the P-V curves for our selected bladder thickness of 0.75mm and our maximum tested thickness of 1.25mm. We use a 3D-printed a bladder holder consisting of an inlet side and a ring that clamps the bladder (Fig. 2c,d), and connect a syringe with water to the holder's inlet, with a pressure sensor (PendoTECH) branched off from that connection. We used the syringe pump to inject 0.2ml of water at a rate of 0.3ml/min, while measuring pressure (Powerlab 16/35, ADInstruments). We selected a thickness of 0.75mm for our bladder as a balance between sufficient holding volume with low upstream pressure ($\sim$20kPa), but high enough stiffness to provide sufficient pressure to push fuel through the reactor line.

B. Characterization Experimental Setup

Our engine characterization setup is shown in Figure 3(a). A regulator (PPR2-N02BG-2, 3-30psi regulator, Pneumatic-Plus) from a wall pressure source is connected to a central fuel tank - a machined Aluminum chamber with an acrylic window. A pressure sensor (Single-use Pressure Sensor, PendoTECH) is connected to the tank. The tank is filled with 50% concentration propulsion-grade hydrogen peroxide (Propulse HTP, Evonik Industries AG). Downstream of the tank, the engine is connected through the fuel line (1/16in ID PVC tubing and duckbill valve). The engine output is connected to a rigid sensorized chamber through an engine adapter cover. The rigid chamber is made of two machined aluminum plates sandwiched on a clear polycarbonate tube (1.75in OD, 200psi rated, McMaster-Carr), sealed by custom-cut Viton gaskets (1/32in thick, McMaster-Carr). The chamber's top lid is modified to include 3D-printed VeroBlue ports for the insertion of another pressure sensor (PendoTECH), a thermocouple (Type-K, Adafruit Industries) and a 30psi safety relief valve (ASME-Code 30psi Relief Valve, McMaster-Carr). Laser-cut acrylic disks were placed inside the chamber to reduce the total internal volume to 21mL from 38mL. Including the tubing, chamber, and engine adapter cover, the total internal volume of the pressurized system is 28mL.

The circuitry hardware includes a prototyping board (METRO 328, Adafruit Industries) for controlling the reactor and exhaust valves through a transistor circuit, where each valve had a separate 12V (reactor valve) and 5V (exhaust valve) power source. The control circuitry sends an output signal to the sensing hardware for synchronizing data and capturing valve input signals. The sensing hardware includes a thermocouple amplifier (MAX31855, Adafruit Industries) connected to another METRO 328 for sensing heat and a PowerLab 16/35 (ADInstruments) for reading the two pressure sensors and the control hardware output signal.

A representative valve control signal for a pressurization cycle is depicted in Figure 3(c). For each cycle in our characterization experiments, there is an injection phase when the reactor valve allows fuel to flow into the reactor, a holding phase where the system is held at a pressurized state, and an exhaust phase when the exhaust valve opens to release gas to atmosphere. For our injection phase, we chose to control our reactor valve flow rate by varying the frequency of a 3ms voltage pulse, from ranges between 10-

Authorized licensed use limited to: MIT. Downloaded on July 04,2025 at 10:25:47 UTC from IEEE Xplore. Restrictions apply.

80Hz (i.e., varying the time between 3ms pulses). The 3ms pulse was the minimal pulse required to get a response from the reactor valve.

C. Actuator Integration Setup

To demonstrate the engine's use in powering actuation, we attach it to two soft actuators through different means. A hard cover with a tubing adapter is added to the engine so it can attach to actuators with tubing interfaces - we attached this to a McKibben actuator. We also directly embed the cap piece into a soft silicone gripper, demonstrating that the engine can be directly integrated into an actuator.

We manufacture our McKibben actuator using a 1/4in braided mesh sleeve (Techflex Inc.), a latex party balloon, Luer connectors, and zip-ties. To obtain an actuator with a rest length of L = 50mm, we follow five steps. First, we cut a section of the mesh to length L + 19mm. Second, we melt the ends of the mesh and zip-tie a Luer connector on one side of the mesh. Third, we cut a party balloon at a length of approximately L + 3mm. Fourth, we insert a Luer connector in the balloon, gluing them together with Sil-Poxy (Smooth-On Inc.). Lastly, we insert the balloon in the mesh, and zip-tie that end. The resulting actuator it holds at least 200kPa, which is within our experimental pressure range.

The silicone gripper was designed for minimal internal volume, which minimizes its actuation time, using a low-volume core casting process described in [26]. We cast a three-finger gripper with Dragon Skin 30 (Smooth-On Inc.) and impregnate fabric sheets on the palm surface as the strain-limiting layers. The gripper has an internal volume of $\sim 5cm^3$ and operating pressure of $\sim 70kPa$. The engine cap is embedded in the gripper inlet using Sil-Poxy.

IV. RESULTS AND DISCUSSIONS

A. Characterization

We first confirm the hypothesized behavior introduced in Figure 1 – that the local fuel bladder allows the LF2C engine to generate pressures above the pressure of the central fuel tank (Fig. 4). Figure 4 shows the pressure inside the rigid chamber after the reactor valve is opened (frequency of 20Hz), allowing the reaction to take place in an LF2C engine and in a modified version that behaves like the traditional F2C architecture discussed previously. The "Traditional" system is implemented by covering the elastic bladder of an LF2C engine, such that fuel flows directly from the central tank into the reactor. In each case, the valve is in its injection phase until the pressurization begins to plateau (2s for LF2C, 4s for Traditional).

Having experimentally confirmed the hypothesized behavior of the LF2C framework, we characterize its response to varying reactor valve inputs, to understand the controllability of our LF2C implementation. We characterize the pressure response for repeatability and delay over multiple cycles, with varying fuel injection rate and fuel injection times. Figure 5 shows the result of the set of characterization experiments, each trial depicting multiple cycles in succession,

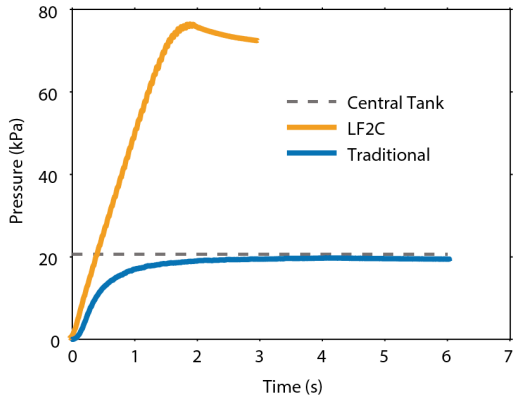

Fig. 4. **Experimental validation of the pressure amplification of the LF2C engine.** Result confirming the hypothesized working principle of the LF2C engine, showing the fuel bladder allows pressurization well above the central tank pressure. Both conditions, "LF2C" and "Traditional," used similar hardware, where "Traditional" was a modified LF2C engine with its bladder covered. In both cases, the central fuel tank was kept at the same pressure.

overlaid from light to dark color, with time zero being the start of the injection phase for each cycle.

The resulting pressure from ten cycles of a 20Hz injection frequency for a 1s injection phase, 2s hold phase, and 2s exhaust phase, starting from a room-temperature reactor is plotted in Figure 5(a). The earlier cycles (in lighter shades), have a lower maximum pressure compared to the later cycles (darker shades) which reach a steady-state maximum pressure. The first cycle shows a substantial delay in pressurization and low maximum pressure, which may be explained by a temperature-driven "warm up" effect in the output of the engine, as the catalyzed decomposition rate of hydrogen peroxide is exponentially proportional to temperature [19], [27]. Starting from room temperature, the engine could have an acceleration stage as the exothermic reaction heats up the system. As shown in other work [27], the heating would eventually reach a temperature equilibrium, causing the convergence in maximum cycle pressure seen in the results. Because it was not possible to directly measure the reactor's temperature, further experiments are needed to confirm this hypothesis.

A closer look at the individual steps during the injection phase is shown in Figure 5(b), and there is a small delay between the incidence of an injection command sent to the valve (reconstructed from the control box output taken during the experiment) and a change in pressurization. This delay, from the first control input, has a mean of 20ms (0.8ms standard deviation), based on readings from 6 cycles. The delays for later control inputs are approximately 10-12ms.

The effect of varying the fuel injection rate on the LF2C's gas output is shown in Figure 5(c). We performed three trials, where the injection frequency is varied for the same number of reactor valve pulses (described in Methods). Namely, 20 reactor valve pulses are delivered at 10, 20, and 40Hz (for injection times of 2, 1, and 0.5s respectively). By keeping the number of valve pulses the same, we assume the total volume

Authorized licensed use limited to: MIT. Downloaded on July 04,2025 at 10:25:47 UTC from IEEE Xplore. Restrictions apply.

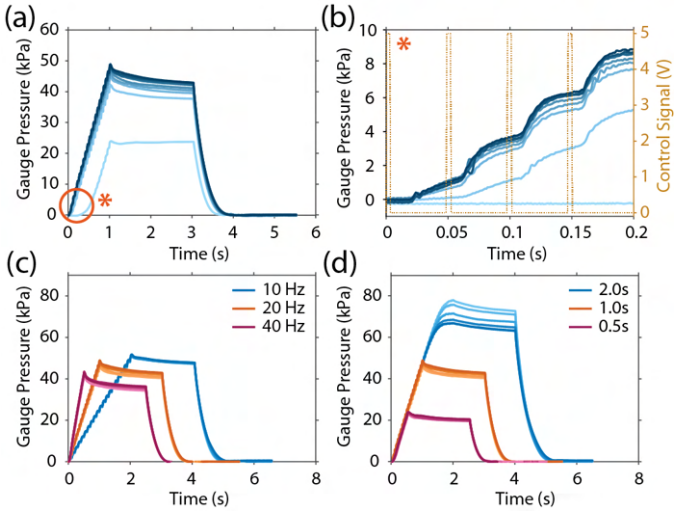

Fig. 5. **Characterization experiments of the engine's response to varying reactor valve inputs.** (a) Pressure response over ten cycles (from light to dark color) for a reactor valve injection phase of 20Hz over 1s. Reactor started from room temperature. (b) Close-up of the injection phase in (a), overlaying the input signal pulses sent to the reactor valve, demonstrating the delay and nonlinear step dynamics for each pulse. (c) Pressure response of the engine for varying injection phase frequencies and same number of injection pulses. Displaying cycles 3-10 for each trial. (d) Pressure response of engine for varying injection times at a 20Hz injection phase, cycles 3-10 displayed.

of injected fuel is similar across trials, though we do not have a measurement of volume. We plot seven cycles from each, discarding the first three "warm-up" cycles described above.

A higher input frequency leads to a faster pressurization rate, evident in the slope of the pressure curve during the injection phase. The pressurization rates are 26 kPa/s for 10Hz, 49 kPa/s for 20Hz, and 86 kPa/s for 40Hz. Fitting the frequency-rate relationship to a linear trend (with a zero-intercept), we find an R^2 value of 0.976, meaning the rate relation can be assumed linear in the studied range. We expect the global trend to be asymptotic, as the system should reach maximum flow by 333Hz (100% duty cycle).

In the 40Hz trial, the engine reaches 37.4kPa at a gas temperature of 24.5°C, after 0.5s of injection. From this, we calculate an output flow for the engine in standard liters per minute (1atm and 0°C) of 4.23SLM. With an engine mass of 36g, this is a flow rate capacity of 141SLM/kg. Based on a previous study with microcompressors weighing between 41g and 333g [17], we find a range between 17 and 63 SLM/kg for compressors. This suggests a 2-8 fold improvement in flow rate for our engine over common microcompressors.

There is also an inverse relationship between frequency and final pressure reached, with a 17% decrease in pressure from 10Hz to 40Hz input. One explanation for this phenomenon is that an increased flow rate leads to a shorter residence time in the reactor, meaning a less complete reaction. Other phenomena might decrease the injection volume with increased rate, such as flow resistances, dynamic responses, or thermal effects. Future work is required to explain this 17% decrease.

Figure 5(d) shows the effect of varying injection time (or total injection cycles) for the same injection frequency, discarding the first three cycles. We varied the injection phase for 0.5, 1, and 2s at 20Hz. The maximum pressure reached is linearly proportional to the injection time, with the 0.5s injection reaching 20kPa and 1s reaching 43kPa. At 2s of injection, we reached the limit of the system as the bladder was emptied, evidenced by the plateauing of the pressure curve before the end of the injection phase.

We also observe that the maximum pressure gradually decreases for each cycle in the 2s case. This is likely a limitation of the experimental hardware. The pressure regulator for the central fuel tank has a slow response, causing a 0.2-0.4KPa pressure drop during each cycle. Based on the bladder PV-curves in Figure 1(c), this pressure drop would cause a 1-5% decrease in bladder volume, which matches the 3-4% decrease in pressure output per cycle. This drifting phenomenon reveals the system's sensitivity to upstream tank pressure at the extremes of its operation.

B. Actuator Integration Demonstrations

In addition to characterizing the response of the engine to various valve inputs, we adapted it to two distinct soft actuation demonstrations, to illustrate its potential and versatility in soft actuation applications. Figure 6 depicts the two demonstrations, and the Supplementary Video includes footage of both. The Methods section explains how the actuators were assembled and interfaced with the engine.

First, we connected our engine to a McKibben actuator, through a plug-and-play tubing interface (Figure 6(a), Supplementary Movie 2). We actuated the system at varying injection rates to demonstrate the LF2C engine's capacity to deliver high pressures (125kPa) (Figure 6(b)) from 1s to 0.2s contraction times. We found a maximum power output of 0.17W, by using video analysis software (Tracker, Open Source Physics) to measure the actuator's displacement of the 500g weight during the fastest contraction. With the engine assembly weighing 36 grams, this gives a specific power minimum of 5W/kg. Accounting for a common McKibben actuator efficiency of 20-30% [28], engine specific power may be as high as 12 or 25W/kg, though more accurate characterization is required in the future. For reference, biological muscle has a specific power of 50-250W/kg [1].

Secondly, we demonstrate a fast-moving soft gripping system actuated by the engine (Figure 6(c), Supplementary Movie 3). With an LED as a reference for start of the valve input, we used slow-motion video to estimate the delay between the control signal and the actuation of the gripper. We found that the actuator began actuation after approximately 30ms after the start of the signal (Figure 6(d)) and fully closed after approximately 230ms (Figure 6(e)).

We recorded the full assembly process of the gripper-embedded engine, to clarify the assembly and demonstrate its simplicity (Supplementary Movie 4).

V. CONCLUSIONS AND FUTURE WORK

In this work, we introduced an approach to localize the fuel storage and fuel reaction within actuators, which can

Authorized licensed use limited to: MIT. Downloaded on July 04,2025 at 10:25:47 UTC from IEEE Xplore. Restrictions apply.

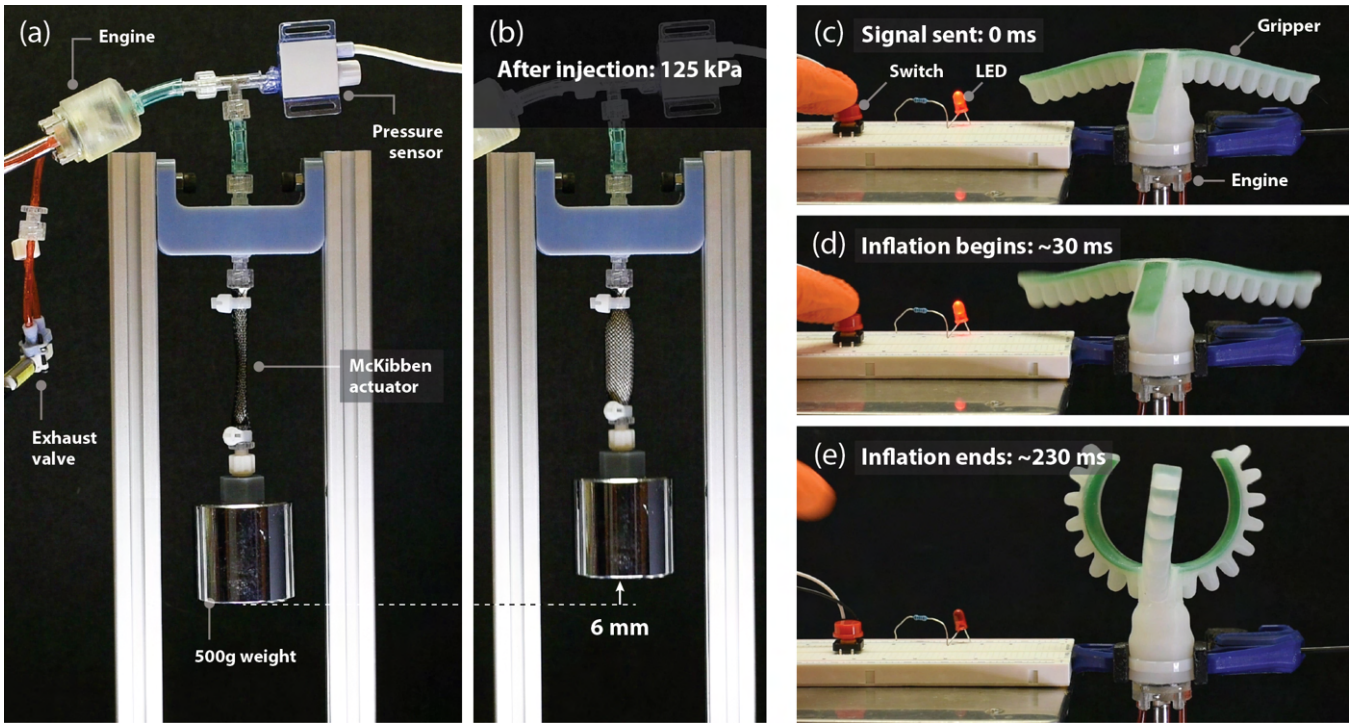

Fig. 6. **Demonstrations of the high-power and high-speed operation of the LF2C engine embedded in soft actuators.** (a) The engine connected to a McKibben actuator, used to lift a 500g calibrated weight. The engine is actuated at varying injection phase frequencies, contracting the actuator at faster rates, used to quantify maximum power output. (b) The McKibben actuator after the fuel injection, inflated at 125kPa and 6mm contraction. (c) The engine, embedded in a silicone gripper, is connected to a circuit that lights an LED at the same time as the actuation signal is sent to the engine, to allow quantification of actuation response time. (d) The gripper starts to inflate ∼30ms after the signal is sent through the switch. (e) The inflation of the gripper ends ∼230ms after the control signal is sent.

generate high pressures at high rates despite a low upstream pressure. We materialized a centimeter-scale implementation of this LF2C strategy using an elastic fuel bladder and a spooled wire catalyst assembly that we can embed into actuators.

We showed experimentally that the LF2C engine is able to generate pressures far above that of the central fuel tank, and characterized the engine's output based on varying reactor valve input signals. By varying the frequency of valve input pulses, we showed that we can reliably change the pressurization rate of the engine, as well as control the system's final pressure value by varying the length of valve operating time. Finally, we demonstrated the engine integrated into two distinct soft actuators - a McKibben actuator via a rigid tube adapter and a silicone gripper via direct embedding. This demonstrated the design's ease of assembly and plug-and-play capabilities in soft robotics.

In the future, we see potential utility for this system in higher performance and untethered applications. Low-pressure, lightweight elastomeric fuel bladders could be used to store large amounts of embodied energy in an untethered platform, a concept championed in [29] for its potential to maximize system-level energy density. On-board battery power for the microcontroller and 5-12V valves would be relatively trivial to implement. Further, the current design is subject to a practical pressure limit, due to the reactor valve's connection to atmospheric pressure. We see potential in surpassing this mechanical limit on maximum pressure by pressure-balancing the reactor valve with the actuator.

Other performance increases could include a small-scale reactor valve embedded in the structure, increased fuel concentration, and optimized reactor design. Trade-offs to explore include varying bladder size and stiffness, reactor size and shape, and tuning the design for the appropriate flow rates, reaction rate, and heat dissipation. Finally, a more complete study can be done on controlling the system.

In addition to these design considerations, in future work we aim to gain insights into the engine's underlying physics, particularly the reactor dynamics, to better understand the apparent "warm-up" phase and the relationship between final pressure and injection rate described in Figure 5.

We posit that propellants have great untapped potential for high-power and long-lifetime untethered pneumatic systems. The LF2C design presented here provides key capabilities toward more modularized, high-speed, high-force, and controllable pneumatic architectures. In the longer term, we envision this architecture to develop into pneumatic artificial muscles with locally stored energy, low-power electrical control, and large amounts of embodied energy [29] fuel storage throughout the body, mimicking the power and control architecture of biological systems.

APPENDIX

Supplementary Video submitted with this paper.

Authorized licensed use limited to: MIT. Downloaded on July 04,2025 at 10:25:47 UTC from IEEE Xplore. Restrictions apply.

ACKNOWLEDGMENTS

This work was funded in part by an MIT MISTI grant, the MIT Mechanical Engineering Department, and the Institute for Medical Engineering Sciences at MIT. S.D.G was funded by the MIT School of Engineering Mathworks Fellowship. A.C. and J.T.B.O. acknowledge the European Union's 2020 ERC-STG under grant agreement No. 948132. M.F. and K.A. were funded by the MIT Summer Research Program.

REFERENCES

[1] M. Li, A. Pal, A. Aghakhani, A. Pena-Francesch, and M. Sitti, "Soft actuators for real-world applications," *Nature Reviews Materials*, vol. 7, pp. 235–249, Mar 2022, epub 2021 Nov 10. [Online]. Available: https://doi.org/10.1038/s41578-021-00389-7

[2] M. T. Tolley, R. F. Shepherd, B. Mosadegh, K. C. Galloway, M. Wehner, M. Karpelson, R. J. Wood, and G. M. Whitesides, "A resilient, untethered soft robot," *Soft Robotics*, vol. 1, no. 3, pp. 213–223, 2014. [Online]. Available: https://doi.org/10.1089/soro.2014.0008

[3] D. Drotman, S. Jadhav, D. Sharp, C. Chan, and M. T. Tolley, "Electronics-free pneumatic circuits for controlling soft-legged robots," *Science Robotics*, vol. 6, no. 51, p. eaay2627, 2021. [Online]. Available: https://www.science.org/doi/abs/10.1126/scirobotics.aay2627

[4] D. Rus and M. T. Tolley, "Design, fabrication and control of soft robots," *Nature*, vol. 521, pp. 467–475, 2015. [Online]. Available: https://doi.org/10.1038/nature14543

[5] E. T. Roche, M. A. Horvath, I. Wamala, A. Alazmani, S.-E. Song, W. Whyte, Z. Machaidze, C. J. Payne, J. C. Weaver, G. Fishbein, J. Kuebler, N. V. Vasilyev, D. J. Mooney, F. A. Pigula, and C. J. Walsh, "Soft robotic sleeve supports heart function," *Science Translational Medicine*, vol. 9, no. 373, p. eaaf3925, 2017. [Online]. Available: https://www.science.org/doi/abs/10.1126/scitranslmed.aaf3925

[6] M. Cianchetti, C. Laschi, A. Menciassi, and P. Dario, "Biomedical applications of soft robotics," *Nature Reviews Materials*, vol. 3, no. 6, pp. 143–153, 2018. [Online]. Available: https://doi.org/10.1038/s41578-018-0022-y

[7] P. Polygerinos, Z. Wang, J. T. Overvelde, K. C. Galloway, R. J. Wood, K. Bertoldi, and C. J. Walsh, "Modeling of Soft Fiber-Reinforced Bending Actuators," *IEEE Transactions on Robotics*, vol. 31, no. 3, pp. 778–789, jun 2015.

[8] D. P. Ferris, J. M. Czerniecki, and B. Hannaford, "An ankle-foot orthosis powered by artificial pneumatic muscles," *Journal of Applied Biomechanics*, vol. 21, no. 2, pp. 189 – 197, 2005. [Online]. Available: https://journals.humankinetics.com/view/journals/jab/21/2/article-p189.xml

[9] J. Nassour, G. Zhao, and M. Grimmer, "Soft pneumatic elbow exoskeleton reduces the muscle activity, metabolic cost and fatigue during holding and carrying of loads," *Scientific Reports*, vol. 11, no. 1, p. 12556, 2021. [Online]. Available: https://doi.org/10.1038/s41598-021-91702-5

[10] B. Katz, J. D. Carlo, and S. Kim, "Mini cheetah: A platform for pushing the limits of dynamic quadruped control," in *2019 International Conference on Robotics and Automation (ICRA)*, 2019, pp. 6295–6301.

[11] H. M. Herr and A. M. Grabowski, "Bionic ankle–foot prosthesis normalizes walking gait for persons with leg amputation," *Proceedings of the Royal Society B: Biological Sciences*, vol. 279, pp. 457–464, 2012. [Online]. Available: http://doi.org/10.1098/rspb.2011.1194

[12] M. Windrich, M. Grimmer, O. Christ, *et al.*, "Active lower limb prosthetics: a systematic review of design issues and solutions," *BioMed Engineering Online*, vol. 15 (Suppl 3), p. 140, 2016. [Online]. Available: https://doi.org/10.1186/s12938-016-0284-9

[13] N. W. Bartlett, M. T. Tolley, J. T. B. Overvelde, J. C. Weaver, B. Mosadegh, K. Bertoldi, G. M. Whitesides, and R. J. Wood, "A 3d-printed, functionally graded soft robot powered by combustion," *Science*, vol. 349, no. 6244, pp. 161–165, 2015. [Online]. Available: https://www.science.org/doi/abs/10.1126/science.aab0129

[14] R. F. Shepherd, A. A. Stokes, J. Freake, J. Barber, P. W. Snyder, A. D. Mazzeo, L. Cademartiri, S. A. Morin, and G. M. Whitesides, "Using explosions to power a soft robot," *Angewandte Chemie International Edition*, vol. 52, no. 10, pp. 2892–2896, 2013. [Online]. Available: https://onlinelibrary.wiley.com/doi/abs/10.1002/anie.201209540

[15] D. Keithly, J. Whitehead, A. Voinea, D. Horna, S. Hollenberg, M. Peck, J. Pikul, and R. F. Shepherd, "A cephalopod-inspired combustion powered hydro-jet engine using soft actuators," *Extreme Mechanics Letters*, vol. 20, pp. 1–8, 2018. [Online]. Available: https://www.sciencedirect.com/science/article/pii/S2352431617301633

[16] C. A. Aubin, R. H. Heisser, O. Peretz, J. Timko, J. Lo, E. F. Helbling, S. Sobhani, A. D. Gat, and R. F. Shepherd, "Powerful, soft combustion actuators for insect-scale robots," *Science*, vol. 381, no. 6663, pp. 1212–1217, 2023. [Online]. Available: https://www.science.org/doi/abs/10.1126/science.adg5067

[17] M. Wehner, M. T. Tolley, Y. Mengüç, Y.-L. Park, A. Mozeika, Y. Ding, C. Onal, R. F. Shepherd, G. M. Whitesides, and R. J. Wood, "Pneumatic energy sources for autonomous and wearable soft robotics," *Soft Robotics*, vol. 1, no. 4, pp. 263–274, 2014. [Online]. Available: https://doi.org/10.1089/soro.2014.0018

[18] M. Goldfarb, E. Barth, M. Gogola, and J. Wehrmeyer, "Design and energetic characterization of a liquid-propellant-powered actuator for self-powered robots," *IEEE/ASME Transactions on Mechatronics*, vol. 8, no. 2, pp. 254–262, 2003.

[19] K. Fite and M. Goldfarb, "Design and energetic characterization of a proportional-injector monopropellant-powered actuator," *IEEE/ASME Transactions on Mechatronics*, vol. 11, no. 2, pp. 196–204, 2006.

[20] K. B. Fite, T. J. Withrow, K. W. Wait, and M. Goldfarb, "A gas-actuated anthropomorphic transhumeral prosthesis," in *Proceedings 2007 IEEE International Conference on Robotics and Automation*, 2007, pp. 3748–3754.

[21] M. A. Bell, B. Gorissen, K. Bertoldi, J. C. Weaver, and R. J. Wood, "A modular and self-contained fluidic engine for soft actuators," *Advanced Intelligent Systems*, vol. 4, no. 1, p. 2100094, 2022. [Online]. Available: https://onlinelibrary.wiley.com/doi/abs/10.1002/aisy.202100094

[22] X. Shen and D. Christ, "Design and control of chemomuscle: A liquid-propellant-powered muscle actuation system," *Journal of Dynamic Systems, Measurement, and Control*, vol. 133, no. 2, p. 021006, 02 2011. [Online]. Available: https://doi.org/10.1115/1.4003208

[23] M. Wehner, R. L. Truby, D. J. Fitzgerald, B. Mosadegh, G. M. Whitesides, J. A. Lewis, and R. J. Wood, "An integrated design and fabrication strategy for entirely soft, autonomous robots," *Nature*, vol. 536, no. 7617, pp. 451–455, 2016. [Online]. Available: https://doi.org/10.1038/nature19100

[24] C. D. Onal, X. Chen, G. M. Whitesides, and D. Rus, *Soft Mobile Robots with On-Board Chemical Pressure Generation*. Cham: Springer International Publishing, 2017, pp. 525–540. [Online]. Available: https://doi.org/10.1007/978-3-319-29363-9_30

[25] S. D. Gollob and E. T. Roche, "Towards a pump-controlled, propellant-powered pneumatic source for untethered soft robots: Modelling and experiments," in *2023 IEEE International Conference on Soft Robotics (RoboSoft)*, 2023, pp. 1–8.

[26] Q. Yu, N. Cao, C. Folinus, and K. P. Becker, "Low-volume cores for fabrication of compact, versatile, and intelligent soft systems," *Advanced Functional Materials*, p. 2404317, 2024.

[27] D. Krejci, A. Woschnak, C. Scharlemann, and K. Ponweiser, "Structural impact of honeycomb catalysts on hydrogen peroxide decomposition for micro propulsion," *Chemical Engineering Research and Design*, vol. 90, no. 12, pp. 2302–2315, 2012. [Online]. Available: https://www.sciencedirect.com/science/article/pii/S0263876212002158

[28] M. A. Meller, M. Bryant, and E. Garcia, "Reconsidering the mckibben muscle: Energetics, operating fluid, and bladder material," *Journal of Intelligent Material Systems and Structures*, vol. 25, no. 18, pp. 2276–2293, 2014. [Online]. Available: https://doi.org/10.1177/1045389X14549872

[29] C. A. Aubin, B. Gorissen, E. Milana, P. R. Buskohl, N. Lazarus, G. A. Slipher, C. Keplinger, J. Bongard, F. Iida, J. A. Lewis, and R. F. Shepherd, "Towards enduring autonomous robots via embodied energy," *Nature*, vol. 602, no. 7897, pp. 393–402, 2022. [Online]. Available: https://doi.org/10.1038/s41586-021-04138-2

Authorized licensed use limited to: MIT. Downloaded on July 04,2025 at 10:25:47 UTC from IEEE Xplore. Restrictions apply.